

The True Parent Phase of $K_{1.9}Fe_{4.2}Se_5$: A Stripe-type Orthorhombic Phase Requiring a Superconducting Distortion

Chih-Han Wang¹, Jie-Yu Yang¹, Wu Phillip M¹, Gwo-Tzong Huang¹, Ming-Jye Wang² and Maw-Kuen Wu^{1*}

¹Institute of Physics, Academia Sinica, Taipei 11529, Taiwan

²Institute of Astrophysics and Astronomy, Academia Sinica, Taipei 10617, Taiwan

* E-mail: mkwu@phys.sinica.edu.tw

Abstract

The origin of the four-fold T_c amplification in $A_xFe_{2-y}Se_2$ (>30 K) compared to FeSe (8 K) remains a central puzzle, complicated by a debate over the true superconducting (SC) parent phase—the $I4/m$ (245) insulating matrix or a supposed $I4/mmm$ metallic phase. Here, we resolve this ambiguity by identifying a novel "stripe-type orthorhombic phase" as the true parent phase of the high- T_c state, whose diffraction signature is the d_2 peaks. Through decisive experiments, we demonstrate that this d_2 parent phase is not intrinsically superconducting. Instead, superconductivity emerges only after this stripe phase undergoes a subsequent structural distortion, the definitive signature of which is the asymmetric broadening of the d_1 main peaks. Our findings establish that the d_2 peaks signal the formation of the parent phase, while the broadening of d_1 peaks signals the transition into the superconducting state. This discovery of a two-step transition—formation of a stripe parent phase, followed by a superconducting distortion—provides a new mechanism for T_c amplification via controlled heterogeneity.

Introduction

A central challenge in unconventional superconductivity is deciphering the intricate relationship between electronic symmetry-breaking states and the superconducting pairing mechanism itself [1-3]. In iron-based superconductors (FeBS), this challenge is embodied by the phenomenon of electronic nematicity—a spontaneous breaking of the C_4 rotational symmetry of the high-temperature tetragonal lattice [4, 5]. This nematic order, however, displays a puzzling dichotomy. In many pnictides, such as the canonical $BaFe_2As_2$ system, nematicity is intertwined with a structural and magnetic ground state that broadly competes with superconductivity [6-8]. In stark contrast, the simplest iron selenide, FeSe ("11" phase), presents a seemingly cooperative relationship: it utilizes a homogeneous nematic transition to host a modest superconducting state at $T_c \approx 8$ K [9-11]. This 8 K baseline in simple FeSe

brings a profound enigma to the forefront when considering the complex, high-Tc $A_x\text{Fe}_{2-y}\text{Se}_2$ ("122") family, which exhibits superconductivity above 30 K [12-14]. The origin of this dramatic, four-fold Tc amplification remains one of the most significant unresolved questions in the field. The system is notoriously complex, dominated by a nanoscale phase separation [15, 16] between a majority, vacancy-ordered, insulating I4/m matrix (the 245 phase, d1 peaks) [17, 18] and a minority metallic phase (d2 peaks) [19, 20]. For over a decade, a prevailing and highly plausible consensus model has been adopted. This model posits that the "extra" Fe atoms—known to be the essential chemical ingredient for superconductivity [21, 22]—are precisely the reagents that form this minority metallic phase. This phase, identified by the d2 peaks, is assumed to adopt an I4/mmm structure [23, 24]. This interpretation is compelling because it provides a direct analogy to the high-Tc pnictides: the parent phase of BaFe_2As_2 is also I4/mmm, and its doped Tc (up to 38K) [6] is remarkably similar to the 31K Tc in the KFe_2Se_2 system. This consensus—that "extra Fe" forms a d2-peak-generating, I4/mmm-like phase which is the 30K superconductor—has been the standard interpretation. However, this paradigm rests on two critical assumptions that, in light of new evidence, may require re-examination: (1) that a distinct, bulk I4/mmm phase actually forms [25], and (2) that its diffraction signature (d2) is intrinsically linked to superconductivity [20]. In this work, we provide data that helps to resolve this ambiguity. We present decisive experiments that complicate this consensus model, demonstrating that the d2 peaks persist even in samples where superconductivity has been suppressed. This motivates us to propose an alternative interpretation. We identify the asymmetric broadening of the d1 peaks as a more direct and unambiguous structural metric for high-Tc superconductivity. We first identify a novel "stripe-type orthorhombic phase" as the true parent phase of the high-Tc state, whose signature is the d2 peaks. Crucially, we then show that this d2 parent phase is not intrinsically superconducting; it requires a second structural distortion—whose definitive signature is the d1 peaks broadening—to activate superconductivity. This "interfacial" model, which evokes the physics of "Superstripes" [26-28], mechanistically links the "chemistry" (the "extra" Fe) to the "physics" (the Tc amplification) [29, 30]. This discovery not only solves the Tc amplification puzzle in the 122 system, but also provides a brand new, universal physical framework for understanding the similar "peak broadening" phenomena observed in other iron-based superconductors, such as BaFe_2As_2 and LaOFeAs [6,31,32].

Results and Discussion

We first analyzed the non-superconducting $\text{K}_2\text{Fe}_4\text{Se}_5$ (245) sample (Fig. 1). The (110) superlattice peak originates from the long-range ordering of Fe vacancies (Fe1 sites), while the (130) reflection corresponds to the nearest-neighbor Fe-Fe planar spacing. As shown in Figure 1A, a sharp transition

is evident between 250 °C and 275 °C, characterized by the suppression of the (110) peak and an abrupt shift in the (130) peak position. This phenomenon has been conventionally interpreted as a structural phase transition from the vacancy-ordered I4/m phase to a vacancy-disordered I4/mmm phase, as schematically depicted in Figure 1C. However, our local structural analysis (Fig. 1B) suggests a more subtle physical mechanism. We propose that the entire transition is driven by the anisotropic thermal expansion and contraction originating at the Fe vacancy (Fe1) site. This anisotropic contraction (upon cooling), in turn, causes a specific, cooperative "left-hand gesture rotation" of the Fe2 atoms (a symmetry-breaking distortion, Fig. 1D left). At the transition (250-275°C), the thermal expansion overcomes this cooperative rotation, causing the Fe2 atoms to "rotate back" into a locally symmetric state (Fig. 1D right). This single event—a local symmetrization driven by thermal expansion—is therefore responsible for both the suppression of the (110) superlattice peak (due to the loss of rotation) and the abrupt jump in the (130) lattice parameters (creating the I4/mmm "illusion"). Crucially, this model also explains the high-temperature behavior. The re-divergence of the D1, D2, and D3 distances above 700°C (Fig. 1B) is driven by simple thermal expansion, which inherently lacks the specific 'left-hand rotation' required to break the symmetry. Therefore, the (110) superlattice peak never reappears. This confirms that the system always retains its fundamental I4/m symmetry, and a true, globally ordered I4/mmm bulk phase does not exist.

We next turn to the superconducting $K_{1.9}Fe_{4.2}Se_5$ (Fe4.2) sample (Fig. 2). This sample provides the key to understanding the mechanism of the 245 phase. In stark contrast to Fig. 1, the (130) reflection does not exhibit an abrupt structural jump. Instead, it undergoes a continuous, dramatic evolution: the intensity is reduced by half, and upon cooling to 200 °C, a distinct secondary peak (d_2) emerges. This directly supports our model: the "extra" Fe atoms (which, as we will show, generate the d_2 peak) act as "pillars" that inhibit the abrupt thermal contraction (the $d(130)$ jump), but critically, do not suppress the global "left-hand gesture rotation" itself, thus allowing the long-range vacancy ordering to persist. Our local structural refinement (Fig. 2B) confirms this, showing that D1, D2, and D3 remain distinctly separated, confirming the persistent I4/m symmetry. Based on these unified observations, we present our model for the d_2 peak's origin in Figure 2D. We propose that when an "extra" Fe atom occupies a vacancy, it inhibits the local thermal contraction and locally locks the structure against the associated rotation. As visualized in Fig. 2D, the purple arrows around the vacancy sites (red d_1 unit) indicate the persisting rotational distortion responsible for the (110) peak. Conversely, the extra Fe atom in the d_2 unit (blue) acts as a pinning center that suppresses this rotation. This creates a locally symmetric (non-rotated) configuration—akin to the high-T configuration in Fig. 2C—which naturally generates a shorter periodicity, $d_2(130)$. This visualization provides the definitive structural explanation for the

"single phase" scenario: the d1 (rotated) and d2 (pinned) states are not separate phases, but are distinct local configurations defined by Fe occupancy on the same continuous I4/m lattice. This coherent coexistence also explains the critical boundary condition at 225°C: at this unique geometry, the changes in D2 and D3 (Fig. 2B/C) cause the diffraction angle to deviate from the required condition (Fig. 2D), leading to destructive interference and explaining why the d2 peak only emerges at 200°C.

We synthesize these atomic-scale distortions (from Fig. 2D) into the formation process of the mesoscopic model shown in Figure 3. As depicted in Figure 3A, the first step is the occupation of a single Fe vacancy, which induces four adjacent orthorhombic distortion cells. Next, as shown in Figure 3B, when another Fe occupies an adjacent vacancy, these local distortions coalesce, initiating the formation of a one-dimensional chain along the [110] direction. Finally, as shown in Figure 3C, this directional alignment of occupied vacancies forms a complete 1D "filament" or "stripe phase". We propose this is an "interphase" embedded between the 245 insulating and 255 metallic domains. At this point, a clear but potentially ambiguous hypothesis emerges: this d₂-peak-generating stripe phase (Fig. 3C) is the superconducting phase. Figure 4 is designed to test this hypothesis and decouple the true structural signatures.

Figure 4A provides the first critical evidence, tuning the system via Fe-content. The main plot (magnetization) reveals a competition between a 125K Charge Ordering (CO) and the superconducting (SC) transition at $T_c \sim 30\text{K}$. As Fe content increases (from Fe_{4.01} to Fe_{4.2}), the 125K CO signature is suppressed, while the SC volume emerges and is enhanced. The inset (XRD) reveals the definitive structural signature. Quantitative fitting of this data (see Fig. S1 and Table S1 in the Supplementary Information) reveals the true 'Step 1' of the transition. Critically, the 100% non-superconducting Fe_{4.01} and Fe_{4.05} samples completely lack the d₂(130) peak. While they already exhibit a d₁/d₁' doublet, the splitting is minimal ($\sim 0.004 \text{ \AA}$), causing their peaks to appear 'sharp'. As Fe content increases (Fe_{4.1} - > Fe_{4.2}), the d₂(130) peak emerges for the first time, the d₁/d₁' splitting simultaneously increases, and superconductivity appears. This establishes the first key link: the emergence of the d₂ parent phase is the essential structural trigger for the onset of superconductivity. Figure 4B then provides the decisive "killer experiment" to decouple the parent phase (d₂) from the superconducting distortion (the broadening), using quenching temperature (TQ) as the tuning parameter. The results show that while high-TQ samples (e.g., 840°C) have a strong SC volume, the SC signal is almost completely suppressed (<1%) as TQ is lowered (e.g., to 650°C). The d₁(130) peak profile correlates perfectly, reverting to a relatively sharp profile (indicating minimal d₁/d₁' splitting). Most critically, the d₂(130) peak—the signature of the very stripe phase we modeled—is clearly observed in all samples, including

the nearly non-superconducting $T_Q=650^\circ\text{C}$ sample. This observation proves that the d_2 peak (the parent phase) is a necessary condition but not the sufficient condition for superconductivity. To quantitatively verify the origin of the broadening, we performed a peak deconvolution, shown in the new Figure 4C. The Triple Lorentzian Fit for the superconducting 840Q sample definitively confirms that the "asymmetric broadening" is not simple disorder, but a superposition of three distinct components: the $d_2(130)$ (parent phase), the main $d_1(130)$ (matrix), and the compressed $d_1'(130)$ (SC phase). This analysis provides direct, quantitative proof for our three-phase coexistence model. This 'two-step transition' model also resolves the paradox of how two different lattices can coexist, which is resolved by the formation of an ordered 'Superstripe' interphase. Figure 4D provides the explicit structural identification for this model. It consists of three key components: (1) The $d_1(245)$ insulating matrix ($a_1 = 8.736\text{\AA}$); (2) The d_2 (interface) phase, our orthorhombic 'stripe' phase (the true parent phase). Crucially, its long axis achieves perfect lattice matching with the d_1 matrix to minimize strain energy, while its contracted short axis gives rise to the $d_2(130)$ peak; and (3) The $d_1'(255)$ metallic phase (the "second distortion" or SC trigger). This framework identifies the asymmetric broadening as the superposition of the d_1 and d_1' peaks. Our 'Expansion/Compression' model explains why this splitting is tuned by T_Q , linking back to our sample synthesis observations. The high-temperature (e.g., 840°C) thermal expansion of the d_1 matrix exerts compressive strain on the embedded d_1' phase. This strain, "frozen in" by quenching, causes the d_1' lattice to become slightly smaller. This mismatch results in the characteristic asymmetric broadening, quantitatively verified in Fig 4C. The degree of this d_1/d_1' splitting, therefore, acts as a direct structural metric for the compressive strain that amplifies the SC volume. To firmly validate our 'Expansion/Compression' model, we examine the microscopic lattice texture of the parent phase shown in Figure 4E. The d_1 matrix is typically treated as a uniform block, but our analysis reveals that its intrinsic Block-AFM order drives a significant periodic modulation along the c -axis. Specifically, the alignment of Fe spins creates local 'cavities' of lattice expansion ($d_{\downarrow\downarrow} = 7.11\text{\AA}$) alternating with regions of contraction ($d_{\uparrow\uparrow} = 6.98\text{\AA}$). This microscopic texture provides the definitive explanation for the superconducting lattice parameters. As the metallic d_1' phase forms, it experiences strong compressive strain in the ab -plane from the rigid matrix. Following the Poisson effect, this ab -plane compression necessitates a compensatory expansion along the c -axis. Figure 4E demonstrates that this expansion is not arbitrary; the d_1' lattice 'locks' precisely into the pre-existing 7.114\AA vertical space provided by the parent magnetic structure. This confirms that the superconductivity in this system is mechanically engineered: the interfacial strain forces the metallic phase to conform to the specific geometric constraints of the parent magnetic scaffold. This "Superstripe" framework (Fig. 4D) also resolves a key apparent contradiction when comparing the

KFeSe system with 122-pnictide systems, such as AFe_2As_2 ($A=Sr, Ca$) [33]. In those pnictide materials, the tetragonal-to-orthorhombic (T-O) structural transition is well-known to release immense strain by forming large, micro-scale "twinning lamellae" or "tweed" structures, which are clearly visible via TEM. A critical question thus arises: if our model also proposes a crucial orthorhombic distortion (the $d1'$ phase), why does the KFeSe system not exhibit this same large-scale, visible twinning? Our model provides a precise and elegant answer. The KFeSe system utilizes a far more sophisticated, nanoscale mechanism to accommodate this strain. As detailed in our Fig. 4D model, the $d2/d1'$ interphase self-organizes by achieving "a-axis lattice matching" with the $d1$ matrix. This mechanism effectively minimizes the strain energy at the interface itself, thereby eliminating the need for the system to form the large, energetically costly micro-scale twins seen in pnictides. Therefore, the absence of such large-scale twinning in KFeSe is not a weakness of our model; rather, it is the strongest experimental evidence confirming the necessity and structural accuracy of our proposed "Superstripe" solution. Therefore, the 'killer experiment' is perfectly clarified: The nearly non-superconducting sample (650Q, Fig 4B) already contains the full 'Superstripe' assembly ($d1$, $d1'$, and $d2$), but the $d1/d1'$ splitting is minimal, indicating low strain. In contrast, the highly superconducting sample (840Q) requires the same assembly but subjected to high compressive strain, which manifests as the significant, broadened $d1/d1'$ splitting

Conclusion

In conclusion, we have resolved the long-standing controversy over the parent phase of superconductivity in $K_xFe_{2-y}S_2$. We demonstrate that the extended debate between the $I4/m$ and $I4/mmm$ phases was based on an incomplete picture. Our model proves that these are not separate phases, but coherent local configurations defined by Fe occupancy on a single, continuous $I4/m$ lattice. We have identified a novel "stripe-type orthorhombic phase," whose signature is the $d2$ peaks, as the true parent phase of the high- T_c state. Crucially, we prove that this $d2$ parent phase is not intrinsically superconducting. It serves as the necessary platform for a subsequent structural distortion; a transition whose definitive signature is the asymmetric broadening of the $d1$ main peaks (indicating $d1/d1'$ coexistence). Our decisive experiments (Fig. 4A and 4B) clearly decouple these two structural events. First, Fig. 4A (Fe-content) proves that the formation of the $d2$ parent phase is the essential 'Step 1' trigger for SC, as the 100% non-superconducting samples (e.g., $Fe_{4.01}$) lack this $d2$ peak entirely. Second, Fig. 4B (TQ-tuning) proves that the parent phase ($d2$ peaks) is not the trigger, as it clearly persists even in the nearly non-superconducting 650Q sample, where the SC-driving distortion (the broadening) is minimal. Furthermore, this "two-step" model—where superconductivity (the $d1'$

distortion) emerges as an interface phenomenon on top of the parent phase ($d1+d2$) which is widely accepted as the anti-ferromagnetic (AFM) insulating state—provides a natural and elegant physical explanation for the long-standing paradox of SC and AFM "coexistence" in this system [34-37]. This discovery of a two-step "parent-to-SC" transition provides a new mechanism for T_c amplification, driven by chemically controlled nanoscale heterogeneity. It mechanistically links the "chemistry" (the "extra" Fe) to the "physics" (the distortion that triggers SC). Crucially, the observation that the superconducting lattice locks precisely into the parent magnetic scaffold confirms that the high- T_c state is structurally engineered by the system's intrinsic geometry. This model not only solves the 122 T_c amplification puzzle and provides a universal framework for "peak broadening" in FeAs-based systems, but it also offers a potential resolution to the long-standing "friend or foe" debate regarding stripes in copper-based superconductors. Our work suggests that static stripes (our $d2$ parent phase) are indeed competitors, but that the interfaces they create are the essential platform (the "friend") required for the subsequent distortion that triggers high- T_c superconductivity.

Experimental Procedures

Sample Synthesis. The $K_2Fe_4Se_5$ (parent phase) and superconducting $K_{1.9}Fe_{4.2}Se_5$ polycrystalline samples were synthesized using a solid-state reaction method, specifically optimized to ensure chemical homogeneity and control the final structural state. High-purity Fe, Se, and K metal plates were mixed according to the target stoichiometry (~ 5 g batches). To ensure uniform precursor mixing, the reagents were subjected to high-energy mechanical ball milling for 60 minutes, a process repeated three times. Aliquots of the resulting powder (~ 0.5 g) were sealed in quartz ampoules backfilled with high-purity argon [38].

Thermal Processing. The thermal history was strictly controlled to isolate the distinct phases:

(1) Parent Phase ($K_2Fe_4Se_5$): Samples were slowly heated to 650°C - 850°C over 7 hours, annealed for 24-30 hours, and subsequently furnace-cooled to room temperature. This slow cooling path ensures the formation of the thermodynamically stable, vacancy-ordered ground state.

(2) Superconducting Phase ($K_{1.9}Fe_{4.2}Se_5$): Samples were inserted directly into a pre-heated furnace set to the desired quenching temperature (TQ, 650°C - 840°C), held for 2 hours for equilibration, and then rapidly quenched into ice water. This fast-cooling protocol is critical to "freeze in" the high-temperature compressive strain at the $d1/d1'$ interface, which we identify as the trigger for superconductivity.

Characterization. High-resolution synchrotron X-ray diffraction (XRD) data were collected at the

National Synchrotron Radiation Research Center (NSRRC), Taiwan. Magnetization measurements were performed using a SQUID magnetometer (Quantum Design). The structural refinements were carried out using the Rietveld method.

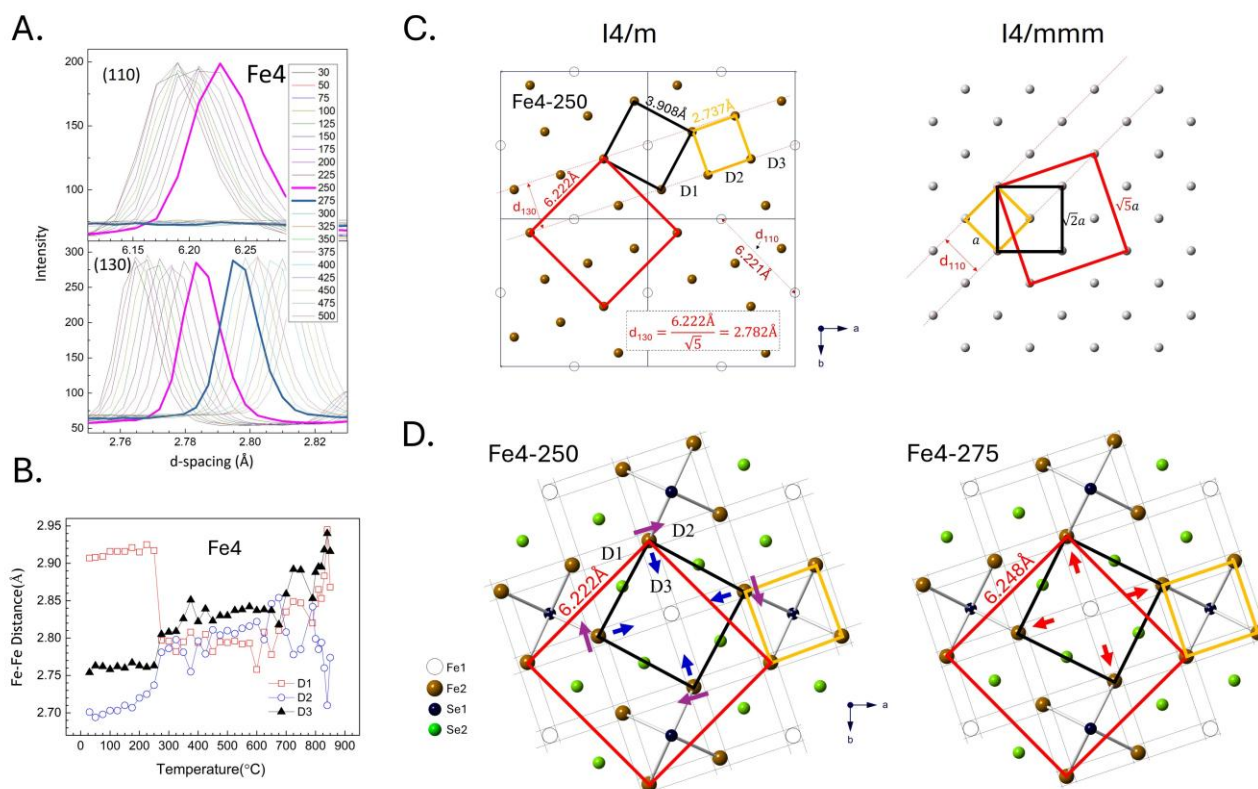


Figure 1. (A) Temperature-dependent XRD patterns of the 245 sample, showing the suppression of the (110) superlattice peak and the abrupt jump of the (130) peak between 250-275°C. (B) The evolution of the three distinct Fe-Fe nearest-neighbor distances (D1, D2, D3), reflecting the thermal expansion/contraction effects at the Fe vacancy site. (C) Schematic illustration of a two-dimensional square lattice comparing unit cell configurations and interatomic distances in the I4/m (left) and I4/mmm (right) phases. (D) Real-space images showing the collective 'left-hand' rotational distortion at 250°C (indicated by arrows)—which is caused by thermal contraction and generates the (110) peak—and the local symmetrization (rotation-back) at 275°C (right panel), which suppresses the (110) peak and creates the I4/mmm "illusion".

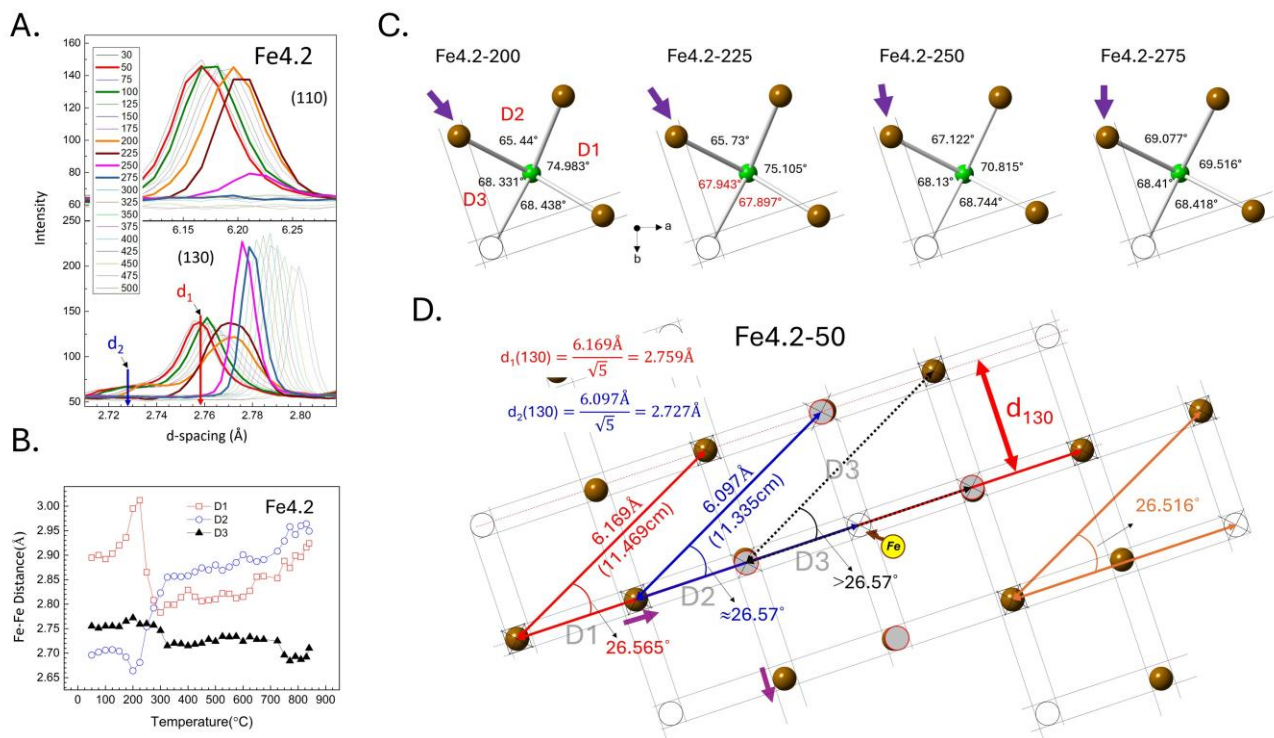


Figure 2 (A) displays the temperature-dependent synchrotron XRD patterns for the superconducting $K_{1.9}\text{Fe}_{4.2}\text{Se}_5$ sample, focusing on the evolution of the (110) and (130) Bragg reflections. **(B)** shows the temperature evolution of the three distinct Fe-Fe nearest-neighbor distances (D1, D2, and D3). The data points were extracted by refining the diffraction patterns at all temperatures using a single $I4/m$ symmetry model, where the d_2 peaks at low temperatures was excluded from the fit. **(C)** illustrates the evolution of the local FeSe_4 tetrahedral geometry. Upon heating from 200 to 275 °C, the tetrahedron becomes progressively more symmetric. This enhancement of the local symmetry at the Fe2 site is directly correlated with the suppression of the (110) superlattice peak (shown in Fig. 2A), as it disrupts the long-range coherence of the Fe vacancy ordering. **(D)** presents a structural model for the superconducting sample at 50 °C, based on the atomic positions refined from XRD data using the $I4/m$ symmetry. The model illustrates the mechanism for the d_2 peak's origin. Crucially, the purple arrows around the vacancy sites (red d1 unit) visualize the 'left-hand rotation' responsible for the (110) peak. In contrast, the extra Fe atom (yellow) in the d2 unit (blue) acts as a pillar that 'pins' the local structure, suppressing this rotation. This creates a locally symmetric, non-rotated state (the d2 phase) that coexists coherently within the rotating $I4/m$ matrix.

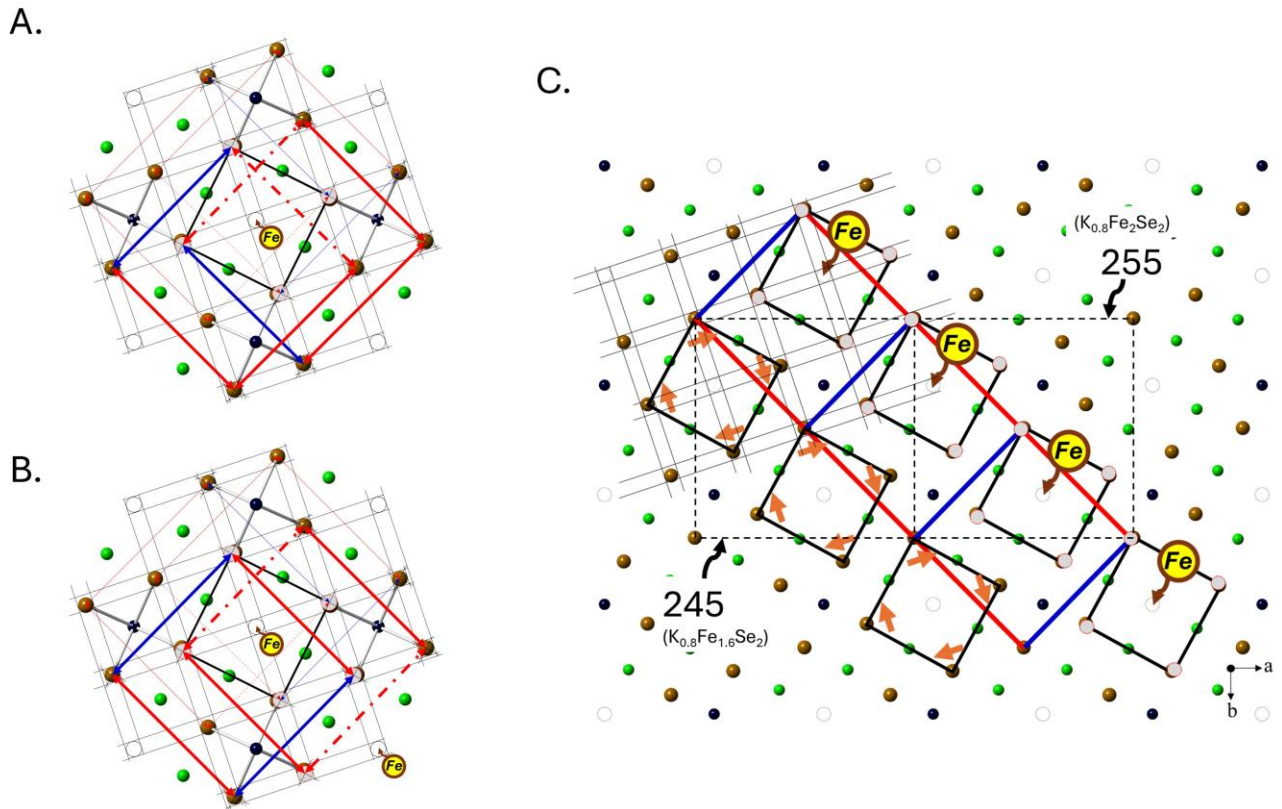


Figure 3 Proposed structural model for the stripe-type orthorhombic interphase. (A) Schematic showing that the occupation of a single Fe vacancy induces four surrounding orthorhombic distortion cells. (B) The occupation of an adjacent vacancy initiates the formation of a one-dimensional, chain-like orthorhombic phase. (C) The directional alignment of these occupied vacancies forms 1D filaments, creating a 'stripe phase'. We propose that this structure is not a separate phase, but an interphase situated between the vacancy-ordered insulating domains (245, $K_{0.8}Fe_{1.6}Se_2$) and the vacancy-filled metallic domains (255, $K_{0.8}Fe_2Se_2$).

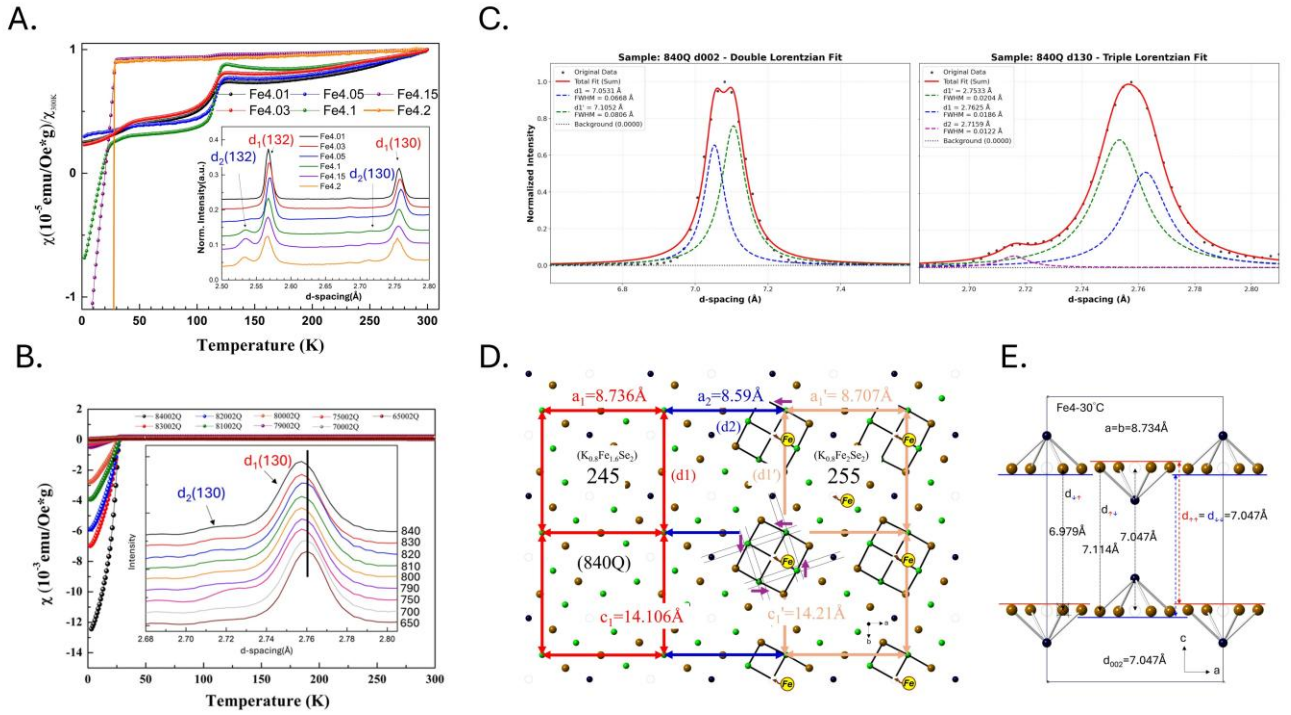


Figure 4. Decoupling the structural signatures of the two-step transition to superconductivity. (A) Magnetization vs. T (main) and XRD (inset) for $K_{1.9}Fe_{4+x}Se_5$ samples with varying Fe content ($x=0.01$ to 0.2). Increasing Fe content suppresses the 125 K charge ordering (CO) transition while enhancing superconductivity (SC). This onset of SC correlates perfectly with the asymmetric broadening of the $d_1(130)$ peak, which signifies the "Step 2" structural distortion. Critically, the non-superconducting (non-SC) Fe4.01 and Fe4.05 samples exhibit only sharp, singular $d_1(130)$ peaks, proving that the $d1/d1'$ coexistence is the essential structural signature for superconductivity. (B) Magnetization vs. T (main) and $d_1(130)$ XRD (inset) for $K_{1.9}Fe_{4.2}Se_5$ subjected to different quenching temperatures (TQ). This is the "killer experiment" that decouples the two structural steps. The nearly non-SC (650Q) sample exhibits a sharp $d_1(130)$ profile (minimal $d1/d1'$ splitting) but clearly retains the $d_2(130)$ peak (quantified in panel C). This definitively proves that the d_2 peak represents the non-superconducting parent phase ("Step 1"). Superconductivity (e.g., in the 840Q sample) only emerges when this parent phase (d_2) undergoes the critical "Step 2" distortion (significant $d1/d1'$ broadening and splitting). (C) Quantitative peak deconvolution (Lorentzian fits) for the superconducting 840Q sample's $d(130)$ profile. This Triple Lorentzian Fit quantitatively confirms that the asymmetric broadening observed in (A) and (B) is not simple disorder, but a superposition of three distinct components: the $d_2(130)$ peak (blue, $\sim 2.716 \text{ \AA}$), the $d_1'(130)$ peak (green, $\sim 2.753 \text{ \AA}$) from the SC phase, and the main $d_1(130)$ peak (red, $\sim 2.762 \text{ \AA}$) from the 245 matrix. This analysis provides definitive proof

for the three-phase ($d_1/d_1'/d_2$) coexistence required for the superconducting state. (D) Real-space structural identification defining the three key components of the "Superstripe" model: d_1 (Red / 245), the insulating 245 matrix ($a_1 \approx 8.736\text{\AA}$); d_2 (Blue), the "stripe-type orthorhombic interphase" (the true parent phase), whose short axis ($\sim 8.59\text{\AA}$) generates the d_2 peak; and d_1' (Orange / 255), the metallic phase representing the "second distortion" (SC trigger). The asymmetric broadening is the signature of the d_1/d_1' coexistence, which is tuned by compressive strain from the high-TQ quenching process. (E) Microscopic origin of the c -axis lattice matching. The intrinsic Block-AFM order within the d_1 matrix (Fe4-30) induces a periodic lattice modulation, creating local c -axis expansions ($d = 7.114\text{\AA}$) and contractions ($d = 6.979\text{\AA}$) around the average value of 7.047\AA . Crucially, the expanded 7.114\AA sites serve as a pre-existing structural template. The metallic d_1' phase, subjected to compressive strain in the ab -plane, expands along the c -axis via the Poisson effect and structurally locks into these magnetically expanded sites.

Reference

1. Keimer B, et al. (2015) From quantum matter to high-temperature superconductivity in copper oxides. *Nature* 518:179-186.
2. Si Q, et al. (2010) Heavy Fermions and Quantum Phase Transitions. *Science* 329:1161-1166.
3. Fradkin E, et al. (2015) Colloquium: Theory of intertwined orders in high temperature superconductors. *Reviews of Modern Physics* 87:457.
4. Fradkin E, et al. (2010) Nematic Fermi fluids in condensed matter physics. *Annual Review of Condensed Matter Physics*. 1:153-178.
5. Fernandes R M, et al. (2014) What drives nematic order in iron-based superconductors? *Nature Physics* 10:97-104.
6. Rotter M, et al. (2008) Superconductivity at 38 K in the iron arsenide $(\text{Ba}_{1-x}\text{K}_x)\text{Fe}_2\text{As}_2$. *Phys Rev Lett* 101:107006.
7. Chu J H, et al. (2010) In-plane resistivity anisotropy in an underdoped iron arsenide superconductor. *Science* 329:824-826.
8. Nandi S, et al. (2010) Anomalous suppression of the orthorhombic lattice distortion in superconducting $\text{Ba}(\text{Fe}_{1-x}\text{Co}_x)_2\text{As}_2$ single crystals. *Phys Rev Lett* 104:057006.
9. Hsu F C, et al. (2008) Superconductivity in the PbO-type structure α -FeSe. *Proc Natl Acad Sci USA* 105:14262-14264.
10. McQueen T M, et al. (2009) Tetragonal-to-orthorhombic phase transition at 90 K in the superconductor $\text{Fe}_{1.01}\text{Se}$. *Phys Rev Lett* 103:057002.
11. Böhmer A E, et al. (2015) Origin of the Tetragonal-to-Orthorhombic Phase Transition in FeSe: A Combined Thermodynamic and NMR Study of Nematicity. *Phys Rev Lett* 114:027001.
12. Guo J, et al. (2010) Superconductivity in the iron selenide $\text{K}_x\text{Fe}_2\text{Se}_2$ ($0 \leq x \leq 1.0$). *Phys Rev B* 82:180520.

13. Krzton-Maziopa A, et al. (2011) Synthesis and crystal growth of $\text{Cs}_{0.8}(\text{FeSe}_{0.98})_2$: a new iron-based superconductor with $T_c = 27$ K. *Journal of Physics: Condensed Matter* 23:052203.
14. Li C H, et al. (2011) Transport properties and anisotropy of $\text{Rb}_{1-x}\text{Fe}_{2-y}\text{Se}_2$ single crystals. *Phys Rev B* 83:184521.
15. Z. Wang, et al. (2015) Archimedean solid like superconducting framework in phase-separated $\text{K}_{0.8}\text{Fe}_{1.6+x}\text{Se}_2$ ($0 \leq x \leq 0.15$). *Phys Rev B* 91:064513.
16. F Chen, et al. (2011) Electronic Identification of the Parental Phases and Mesoscopic Phase Separation of $\text{K}_x\text{Fe}_{2-y}\text{Se}_2$ Superconductors. *Phys Rev X* 1:021020.
17. Alessandro Ricci, et al. (2011) Intrinsic phase separation in superconducting $\text{K}_{0.8}\text{Fe}_{1.6}\text{Se}_2$ ($T_c = 31.8$ K) single crystals. *Supercond. Sci. Technol.* 24:082002.
18. Wei Bao, (2015) Structure, magnetic order and excitations in the 245 family of Fe-based superconductors. *J. Phys.: Condens. Matter* 27:023201.
19. Wei Li, et al. (2012) Phase separation and magnetic order in K-doped iron selenide superconductor. *Nature Physics* 8:126-130.
20. Wei Li, et al. (2012) KFe_2Se_2 is the Parent Compound of K-Doped Iron Selenide Superconductors. *Phys Rev Lett* 109:057003.
21. Xiixin Ding, et al. (2013) Influence of microstructure on superconductivity in $\text{K}_x\text{Fe}_{2-y}\text{Se}_2$ and evidence for a new parent phase $\text{K}_2\text{Fe}_7\text{Se}_8$. *Nature Communications* 4:1897.
22. Wang C H, et al. (2019) Role of the extra Fe in $\text{K}_{2-x}\text{Fe}_{4+y}\text{Se}_5$ superconductors. *Proc Natl Acad Sci USA* 116:1104-1109.
23. N. Lazarević, et al. (2012) Vacancy-induced nanoscale phase separation in $\text{K}_x\text{Fe}_{2-y}\text{Se}_2$ single crystals evidenced by Raman scattering and powder x-ray diffraction. *Phys Rev B* 86:054503.
24. Z. Wang, et al. (2011) Microstructure and ordering of iron vacancies in the superconductor system $\text{K}_y\text{Fe}_x\text{Se}_2$ as seen via transmission electron microscopy. *Phys Rev B* 83:140505(R).
25. Y. Liu, et al. (2012) Evolution of precipitate morphology during heat treatment and its implications for the superconductivity in $\text{K}_x\text{Fe}_{1.6+y}\text{Se}_2$ single crystals. *Phys Rev B* 86:144507.
26. Bianconi A, et al. (2013) Superstripes and Superconductivity in Complex Granular Matter. *J Supercond Nov Magn* 26:2585-2588.
27. Campi G, et al. (2015) Inhomogeneity of charge-density-wave order and quenched disorder in a high- T_c superconductor. *Nature* 525:359-362.
28. Tranquada J M, et al. (1995) Evidence for stripe correlations of spins and holes in copper oxide superconductors. *Nature* 375:561-563.
29. Chunruo Duan, et al. (2018) Appearance of superconductivity at the vacancy order-disorder boundary in $\text{K}_x\text{Fe}_{2-y}\text{Se}_2$. *Phys Rev B* 97:184502.
30. G Campi, et al. (2025) Microstructure Morphology of Chemical and Structural Phase Separation in Thermally Treated $\text{K}_x\text{Fe}_{2-y}\text{Se}_2$ Superconductor. *ChemPhysChem* 26:e202400363.
31. Marianne Rotter, et al. (2008) Superconductivity and Crystal Structures of $(\text{Ba}_{1-x}\text{K}_x)\text{Fe}_2\text{As}_2$ ($x=0-1$). *Angew. Chem. Int. Ed.* 47:7949-795.

32. Clarina de la Cruz, et al. (2008) Magnetic order close to superconductivity in the iron-based layered $\text{LaO}_{1-x}\text{F}_x\text{FeAs}$ systems. *Nature* 453:899-902.
33. C Ma, et al. (2009) Microstructure and tetragonal-to-orthorhombic phase transition of AFe_2As_2 (A=Sr, Ca) as seen via transmission electron microscopy. *Phys Rev B* 79:060506.
34. Z Shermadini, et al. (2011) Coexistence of Magnetism and Superconductivity in the Iron-Based Compound $\text{Cs}_{0.8}(\text{FeSe}_{0.98})_2$. *Phys Rev Lett* 106:117602.
35. Bao Wei, et al. (2011) A Novel Large Moment Antiferromagnetic Order in $\text{K}_{0.8}\text{Fe}_{1.6}\text{Se}_2$ Superconductor. *Chin. Rev Lett* 28: 086104.
36. Despina Louca, et al. (2013) The hybrid lattice of $\text{K}_x\text{Fe}_{2-y}\text{Se}_2$: where superconductivity and magnetism coexist. *Scientific Reports* 3:2047.
37. F Ye, et al. (2011) Common Crystalline and Magnetic Structure of Superconducting $\text{A}_2\text{Fe}_4\text{Se}_5$ (A = K, Rb, Cs, Tl) Single Crystals Measured Using Neutron Diffraction. *Phys Rev Lett* 107:137003.
38. Wang C H et al. (2015) Disordered Fe vacancies and superconductivity in potassium-intercalated iron selenide ($\text{K}_{2-x}\text{Fe}_{4+y}\text{Se}_5$). *Europhys Lett* 111:27004.

Supplementary Information

Sample	d1' Center (Å)	d1' FWHM (Å)	d1 Center (Å)	d1 FWHM (Å)	d2 Center (Å)	d2 FWHM (Å)
Fe4.2	2.7525	0.0144	2.7593	0.0123	2.7114	0.0102
Fe4.15	2.7531	0.0141	2.7598	0.0128	2.7128	0.0095
Fe4.1	2.7542	0.0121	2.7602	0.0114	2.7136	0.0080
Fe4.05	2.7575	0.0100	2.7626	0.0100	—	—
Fe4.03	2.7562	0.0103	2.7616	0.0102	—	—
Fe4.01	2.7556	0.0100	2.7596	0.0100	—	—

Table S1. Quantitative fit parameters from the Lorentzian Fits of the d(130) XRD peaks for the Fe-content series (Fig. 4A). The parameters (Center, FWHM) for d1', d1, and d2 were extracted. Note that the d₂(130) peak is entirely absent (—) in the non-superconducting samples (Fe4.01, Fe4.03, Fe4.05) and emerges only at the onset of superconductivity (Fe4.1).

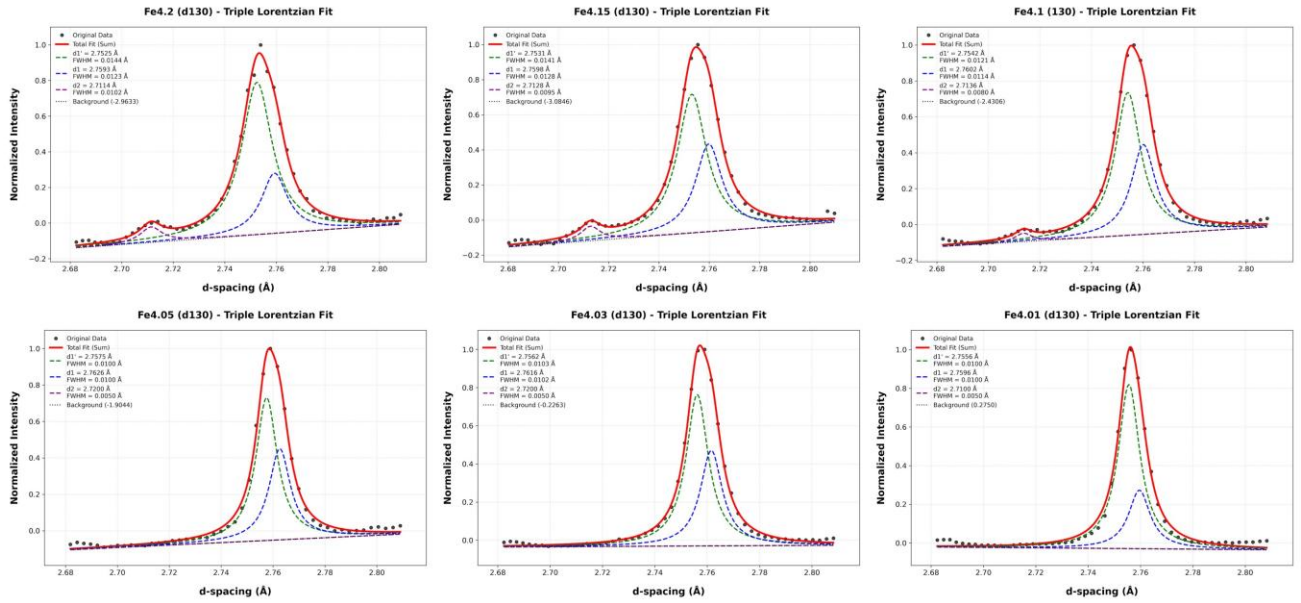


Figure S1. Quantitative deconvolution of the d(130) XRD profiles for the Fe-content series (Fig. 4A). These fits provide direct visual proof for the "Step 1" transition. The $d_2(130)$ peak (blue dashed line, ~ 2.71 Å) is completely absent in the non-superconducting samples (bottom row, Fe4.01-Fe4.05) and clearly emerges at the onset of superconductivity (top row, Fe4.1-Fe4.2), correlating with the suppression of CO and the increase in d_1/d_1' splitting.

d130 (Sample)	d1' - Center (Å)	d1' - FWHM (Å)	d1 - Center (Å)	d1 - FWHM (Å)	d2 - Center (Å)	d2 - FWHM (Å)
650Q	2.7563(6)	0.0179(9)	2.7649(6)	0.0153(12)	2.7167(23)	0.0127(82)
700Q	2.7557(7)	0.0184(10)	2.7646(7)	0.0155(14)	2.7166(22)	0.0134(80)
750Q	2.7542(10)	0.0202(15)	2.7633(9)	0.0163(19)	2.7230(8)	0.0156(30)
790Q	2.7546(6)	0.0197(9)	2.7637(7)	0.0173(13)	2.7155(12)	0.0169(45)
800Q	2.7540(8)	0.0202(11)	2.7629(8)	0.0172(17)	2.7157(12)	0.0163(44)
810Q	2.7541(7)	0.0201(11)	2.7637(7)	0.0173(15)	2.7152(13)	0.0156(47)
820Q	2.7544(7)	0.0203(9)	2.7637(7)	0.0192(11)	2.7150(8)	0.0094(28)
830Q	2.7538(7)	0.0192(10)	2.7626(7)	0.0171(13)	2.7158(10)	0.0131(37)
840Q	2.7533(7)	0.0204(11)	2.7625(8)	0.0186(14)	2.7159(10)	0.0122(35)

Table S2. Quantitative fit parameters from the Lorentzian Fits of the d(130) XRD peaks for the TQ-tuning series (Fig. 4B). The parameters (Center, FWHM) for d_1' , d_1 , and d_2 were extracted. Note that the $d_2(130)$ peak (Center ≈ 2.716 Å) is consistently present in all samples, including the nearly non-SC 650Q. Furthermore, the $d_1'(130)$ Center position systematically shifts to a smaller d-spacing (lattice contraction) as TQ increases (from 2.7563 Å at 650Q to 2.7533 Å at 840Q), providing quantitative proof of the compressive strain model.

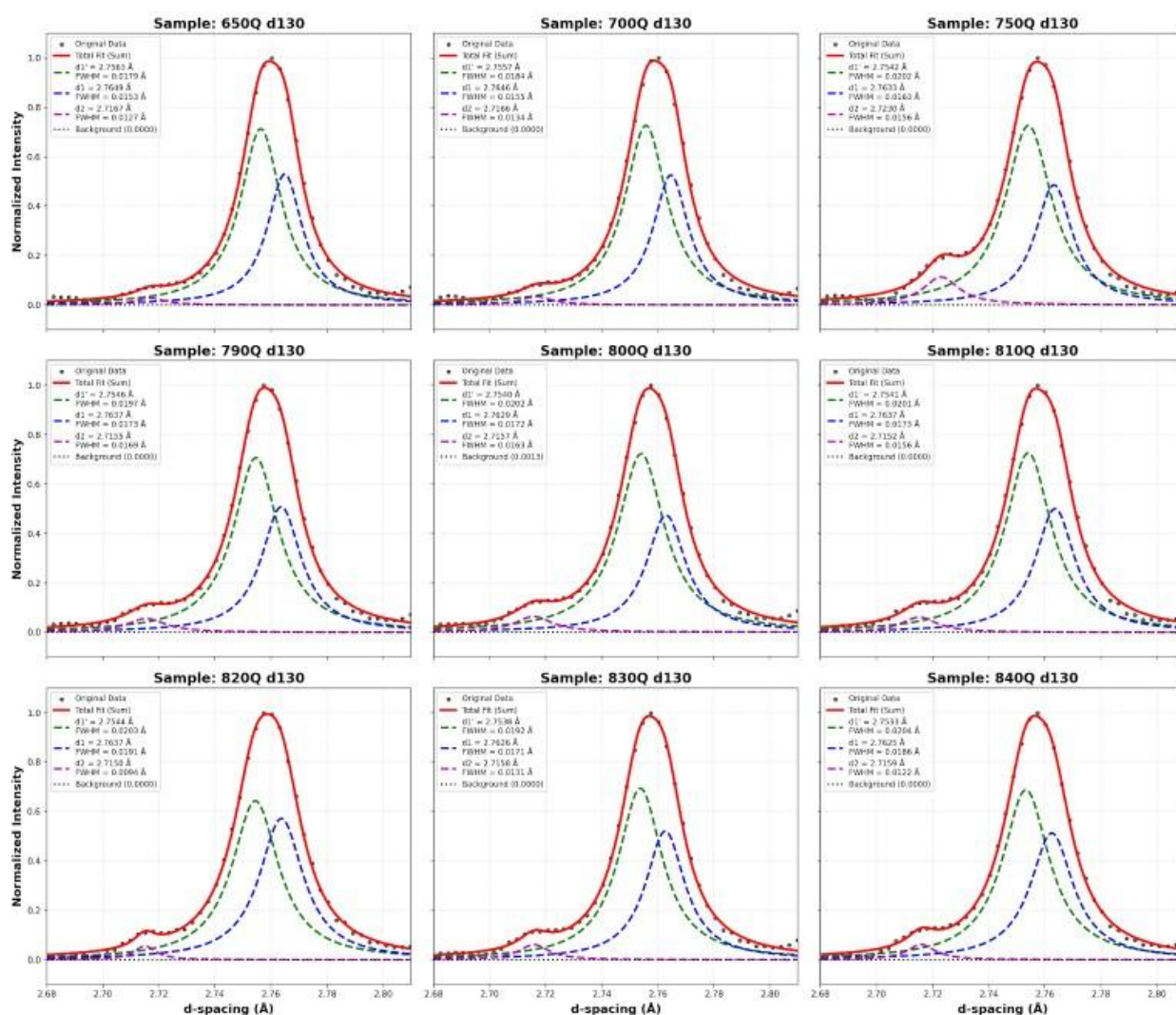


Figure S2. Quantitative deconvolution of the $d(130)$ XRD profiles for the TQ-tuning series (Fig. 4B). These fits provide the visual proof for the "Step 2" (physical distortion) mechanism. They clearly show that the $d_2(130)$ peak (blue dashed line, ~ 2.71 Å) persists in all samples, confirming it is the non-SC parent phase. The broadening of the main peak is confirmed to be a $d1/d1'$ doublet, whose separation is tuned by TQ (compressive strain).

d002 (Sample)	d1 - Center (Å)	d1 - FWHM (Å)	d1' - Center (Å)	d1' - FWHM (Å)
650Q	7.041(3)	0.068(9)	7.093(4)	0.086(8)
700Q	7.047(3)	0.071(8)	7.100(4)	0.086(8)
750Q	7.046(3)	0.071(7)	7.098(3)	0.080(7)
790Q	7.050(3)	0.070(8)	7.103(4)	0.086(8)
800Q	7.050(3)	0.069(8)	7.103(4)	0.085(8)
810Q	7.053(3)	0.069(8)	7.106(4)	0.085(7)
820Q	7.058(3)	0.069(8)	7.111(4)	0.085(7)
830Q	7.050(3)	0.068(8)	7.102(4)	0.084(8)
840Q	7.053(3)	0.068(8)	7.105(4)	0.084(7)

Table S3. Quantitative fit parameters from the Lorentzian Fits of the d(002) XRD peaks for the TQ-tuning series (Fig. 4B). The parameters show that the c-axis peak (002) also experiences a d1/d1' splitting. This splitting correlates with TQ (e.g., d1'-Center trends from 7.093 Å at 650Q to 7.105 Å at 840Q), providing further support for the 3D nature of the compressive strain.

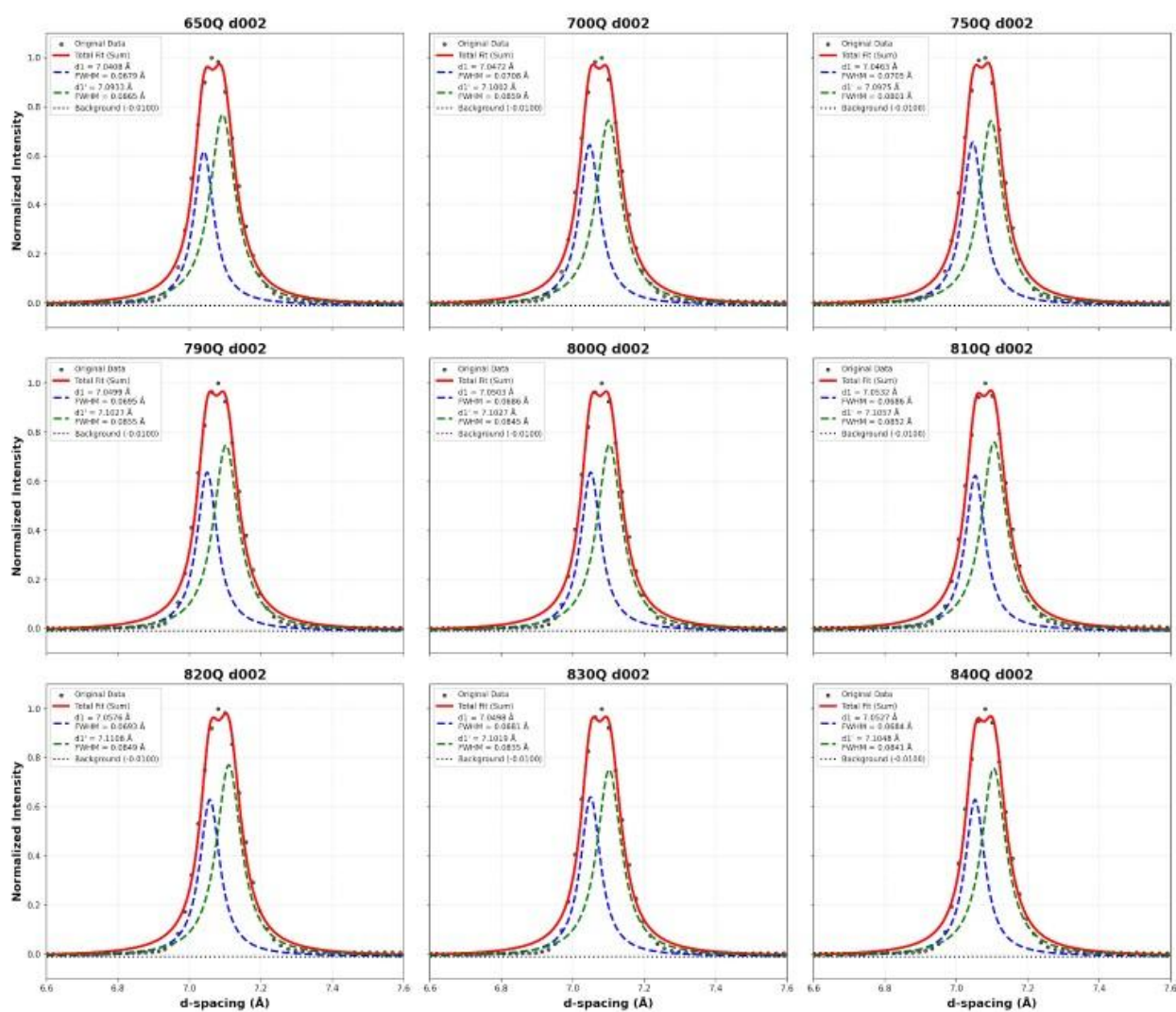


Figure S3. Quantitative deconvolution of the d(002) XRD profiles for the TQ-tuning series (Fig. 4B). These fits provide visual confirmation of the d1/d1' splitting along the c-axis, as detailed in Table S3.

Table S4: The structural information for $K_{2-x}Fe_{4+y}Se_5$ as Rietveld refinement from the synchrotron diffraction data.

250°C						K ₂ Fe ₄ Se ₅						275°C					
a (Å) = 8.798503		c (Å) = 14.175853		$\alpha=\beta=\gamma=90^\circ$		a (Å) = 8.835796		c (Å) = 14.125487		$\alpha=\beta=\gamma=90^\circ$							
	x	y	z	mult.	Occ.		x	y	z	mult.	Occ.		x	y	z	mult.	Occ.
K ₁ (2b)	0	0	0.5	2	0.837	K ₁ (2b)	0	0	0.5	2	0.699						
K ₂ (8h)	0.822215	0.394461	0.5	8	0.715	K ₂ (8h)	0.820033	0.376845	0.5	8	0.787						
Fe ₁ (4d)	0	0.5	0.25	4	0.056	Fe ₁ (4d)	0	0.5	0.25	4	0.823						
Fe ₂ (16i)	0.300259	0.407910	0.248050	16	1.029	Fe ₂ (16i)	0.301263	0.399740	0.250456	16	0.831						
Se ₁ (4e)	0	0	0.139953	4	1.052	Se ₁ (4e)	0	0	0.140435	4	1						
Se ₂ (16i)	0.111857	0.297989	0.353579	16	1.019	Se ₂ (16i)	0.099966	0.299369	0.352954	16	1.02						
Rwp = 3.94% , Rp = 2.65% , $\chi^2 = 0.1346$						Space group: I4/m						Rwp = 3.3% , Rp = 2.07% , $\chi^2 = 0.09938$					

(83.06%)						1.9(Fe _{4.2})5-50°C						(16.94%)					
a (Å) = 8.724023		c (Å) = 14.149008		$\alpha=\beta=\gamma=90^\circ$		a (Å) = 3.849780		c (Å) = 14.239380		$\alpha=\beta=\gamma=90^\circ$							
	x	y	z	mult.	Occ.		x	y	z	mult.	Occ.		x	y	z	mult.	Occ.
K ₁ (2b)	0	0	0.5	2	0.812	K ₁ (2b)	0	0	0	2	0.406						
K ₂ (8h)	0.819124	0.389778	0.5	8	0.656	Fe ₁ (4d)	0	0.5	0.25	4	1						
Fe ₁ (4d)	0	0.5	0.25	4	0.144	Se ₁ (4e)	0	0	0.355627	4	1						
Fe ₂ (16i)	0.301959	0.407584	0.249950	16	1												
Se ₁ (4e)	0	0	0.138161	4	1												
Se ₂ (16i)	0.111241	0.299533	0.353356	16	1												
						Rwp = 3.08% , Rp = 2.33% , $\chi^2 = 0.07341$						Space group: I4/m					

245-30°C

245-30°C					
a (Å) = 8.734420		c (Å) = 14.093736		$\alpha=\beta=\gamma=90^\circ$	
	x	y	z	mult.	Occ.
K ₁ (2b)	0	0	0.5	2	0.794
K ₂ (8h)	0.821649	0.393774	0.5	8	0.707
Fe ₁ (4d)	0	0.5	0.25	4	0.046
Fe ₂ (16i)	0.301557	0.408172	0.247605	16	0.999
Se ₁ (4e)	0	0	0.137044	4	1.018
Se ₂ (16i)	0.111857	0.298674	0.354210	16	0.980
Rwp = 4.17% , Rp = 2.86% , $\chi^2 = 0.1459$ Space group: I4/m					